



Necking behavior of AA 6022-T4 based on the crystal plasticity and damage models



Jong-Bong Kim^a, Jeong Whan Yoon^{b,*}

^a Department of Mechanical and Automotive Engineering, Seoul National University of Science and Technology, Gongneung-ro 232, Nowon-Gu, Seoul 139-743, Republic of Korea

^b Faculty of Science, Engineering and Built Environment, Deakin University, Geelong Waurn Pond, VIC 3220, Australia

ARTICLE INFO

Article history:

Received 13 September 2014

Received in revised form 13 May 2015

Available online 2 July 2015

Keywords:

B. Crystal plasticity

Texture

ABSTRACT

In order to analyze necking behavior with a continuum level approach, initial imperfection or bifurcation algorithm should be employed. The initial imperfection is arbitrary and has a great effect on the necking behavior of sheet metals. Most polycrystalline materials have natural imperfection such as orientation mismatches across the grain boundaries. In polycrystal plasticity, orientation mismatch is considered as material imperfection instead of geometric imperfection including thickness unevenness. The main idea of this study is to investigate the possibility that the stress concentration on a grain boundary (caused by orientation mismatch) works as imperfection and finally causes necking. For the consideration of stress concentration along grain boundaries, a crystal plasticity model was introduced in three-dimensional finite element analysis of a tensile test. A small region of a tensile specimen was divided into sufficient number of octahedral grains and each grain was discretized by fine tetrahedron elements. The same orientation angle was allocated for all the elements in each grain, but different orientations for grain by grain. Using this crystal plasticity-based analysis, stress concentration in the grain boundaries can be predicted. Also, four damage models based on the critical strain and stress were proposed to consider material softening due to void initiation and growth under the framework of crystal plasticity theory. The damage parameters for each model were determined based on the stress–strain relations obtained from experiment. Void nucleation, growth and coalescence behaviors during necking were reasonably predicted. Finally, the predicted necking behaviors of AA 6022-T4 were compared with the experimental results in terms of necking strain, deformed shape, and necking direction.

© 2015 Elsevier Ltd. All rights reserved.

1. Introduction

Finite element analysis based on crystal plasticity model is widely used to understand the plastic behaviors of materials. Most researches have been focused on developing the constitutive relations of single crystal (Kim and Oh, 2003; Borg, 2007; Li et al., 2008) and polycrystalline materials (Dao and Asaro, 1996; Yoon et al., 2005; Zamiri et al., 2007; Li et al., 2004, 2008). Yoon et al. (2005) investigated the anisotropic hardening behavior of cube textured aluminum alloy sheets using a crystal plasticity model. Recently, various studies have been carried out predicting the twinning behavior of hexagonal close packed

* Corresponding author.

E-mail address: j.yoon@deakin.edu.au (J.W. Yoon).

(HCP) materials (Choi et al., 2010; Zhang et al., 2007; Bridier et al., 2009; Beausir et al., 2007; Knezevic et al., 2010; Wang et al., 2010, 2013). Among them, Choi et al. (2010) analyzed the stress concentration at the grain boundary and the twinning behaviors of magnesium alloys. They allocated the grain orientation obtained from electron backscatter diffraction (EBSD) to a regular element. Knezevic et al. (2010) investigated effect of anisotropic strain hardening on twinning behavior of AZ31 using three-dimensional crystal plasticity finite element method.

For computational effectiveness, crystal plasticity finite element analyses were sometimes carried out in two-dimensional plane stress or plane strain framework. However, 2D analysis is not capable of predicting three dimensional deformations including out of plane (Rossiter et al., 2010). Moreover, the localized deformation after necking is three dimensional, and this localized deformation cannot be properly modeled in 2D analysis (Simha et al., 2008). In this study, the necking behavior of AA 6022-T4 is analyzed using crystal plasticity finite element method (CPFEM) in three-dimensional framework. Using a conventional finite element method based on continuum mechanics, a localized necking cannot be predicted without initial imperfections (Marciniak and Kuczynski, 1967; Wang et al., 2011; Bettaieb and Abed-Meraim, 2015) or bifurcation algorithm (Hill and Hutchinson, 1975; Okazawa, 2010; Yoshida and Kuroda, 2012). However, in crystal plasticity-based finite element analysis, the stress concentration from orientation mismatch near the grain boundaries can cause initial voids and initiate the localized deformation. In polycrystalline metals, each grain has its own orientation. Therefore, the orientation of one grain does not coincide with that of its neighboring grains and stress concentration may take place during deformation. To analyze the stress concentration near grain boundaries during necking, crystal plasticity finite element method is introduced by conducting tensile test simulation.

There are small and large scale CPFEM regarding the scale of volume a material point represents. A recent comprehensive review of CPFEM is done by Roters et al. (2010). In small scale CPFEM simulations, the size of the finite element mesh is equal to or smaller than the grain size. With such sub-grain resolutions, heterogeneity of deformation with a single crystal is taken into account (Zhang et al., 2009; Saito et al., 2012; Mayeur et al., 2013; Rossiter et al., 2013; Sabnis et al., 2013; Eisenlohr et al., 2013; Choi et al., 2013, 2014). Large scale refers to simulations with more than one crystal assigned to one integration point and the number of grains is usually large enough to study the average behavior of the material such as the texture evolution. Homogenization schemes are needed to connect a material point to each constituent grain. Commonly used homogenization schemes were described in detail in the literatures by Lebensohn and Tomé (1993), Segurado et al. (2012) and Qiao et al. (2014). Especially, a crystal plasticity-based forming limit prediction in large scale CPFEM approach was presented by Inal et al. (2005), Neil and Agnew (2009) and Franz et al. (2013). Effect of grain orientation on sheet necking was investigated by Wu et al. (2007).

Asaro and Needleman (1985) showed that localized plastic deformation is strongly influenced by microstructure. In many studies of crystal plasticity finite element method it is assumed that many grains exist in an element and homogenization or averaging scheme is used to integrate a single crystal constitutive relation into a polycrystalline constitutive relation (Zamiri et al., 2007; Yoon et al., 2005; Dao and Li, 2001). Using a homogenization scheme in a large scale CPFEM, therefore, the size of an element can be far greater than the one of a grain, and a large scale problem such as sheet forming can be analyzed. However, the localized deformation and stress concentration between grains cannot be predicted using a homogenization method. To overcome this difficulty, Wang et al. (2011) introduced initial imperfections, proposed by Marciniak and Kuczynski (1967), to predict the localized necking and forming limit diagram (FLD) for a magnesium alloy sheet using crystal plasticity finite element method.

In this study, grains are discretized into fine elements in order to describe the stress concentration near grain boundaries and to predict the localized necking deformation. In the current approach, a large scale problem such as sheet metal forming cannot be solved because of computational power including computer memory and computation time. However, the initiation and progress of necking can be predicted in detail. Rossiter et al. (2010) also discretized a grain using many elements and simulated material deformation in three-dimensional microstructure. They used the microstructure information obtained from EBSD and investigated the effects of strain rate, strain path, and thermal softening on the formation of localized deformation. Kanjarla et al. (2010) also discretized grains using many elements and investigated the plastic deformation fields near the grain boundaries and influence of grain interaction on intra-grain deformations. Lin et al. (2011) also modeled the grains near crack tips using finite elements and predicted a crack propagation path under cyclic loads. In this study, each grain is discretized by sufficient number of elements and, then a large deformation up to necking is analyzed using crystal plasticity finite element method with damage models. Void nucleation, growth and coalescence behaviors are investigated.

Without the consideration of damage evolution, i.e. material softening due to damage, a sudden drop of load carrying capacity after necking during tensile tests cannot be described by finite element analysis (Nielsen and Tvergaard, 2009). There are two main approaches to damage mechanics. The first one is a micromechanics-based damage model that was proposed by Gurson (1975). In micromechanics-based approach (Gurson, 1975; Tvergaard and Needleman, 1984; Zhang et al., 2000), damage evolution was described by void nucleation, growth and coalescence. Void nucleation and growth are modeled and the related coefficients have to be determined using experimental data. Nielsen and Tvergaard (2009) successfully analyzed the necking and fracture behavior of friction stir welded sheets using the modified Gurson model (Tvergaard and Needleman, 1984). The other approach to damage analysis is the Continuum Damage Mechanics (CDM). In CDM frameworks (Cockcroft and Latham, 1968; Johnson and Cook, 1985; Lemaitre, 1985; Lemaitre and Chaboche, 1990), fracture strain is determined using stress, pressure, temperature, and stress triaxiality. After these studies, many improved models were proposed to include the effect of Lode angle (Teng, 2008; Xue, 2009; Malcher et al., 2012, 2013) and anisotropic damage (Ekh et al., 2004; Mengonia and Ponthot, 2014). Malcher and Mamiya (2014) proposed an improved damage evolution law by developing a denominator of damage function.

In addition to these studies, there were a few recent researches about damage incorporating CPFEM. Bieler et al. (2009) showed the role of heterogeneous deformation on damage nucleation at the grain boundaries in single phase metals. Recently, Tasan et al. (2014) showed the strain localization and damage in dual phase steels by coupled in-situ experiment and crystal plasticity simulation. Nguyen et al. (2015) proposed a nonlocal coupled damage-plasticity model for the analysis of ductile failure.

In this study, several simple damage models are proposed with the function of critical shear strain, maximum shear strain, effective strain, principal strain etc within the framework of CPFEM. Therefore, the damage models used in this study are based on Continuum Damage Mechanics (CDM). However, the void initiation, growth and coalescence behavior can be predicted by incorporating CPFEM. Furthermore, the material weakening from damage is used to describe a sudden drop of load carrying capacity after necking. In the previous works by the authors (Kim et al., 2012; Kim and Yoon, 2013), the possibility of necking prediction by CPFEM was briefly explored using 2D shaped grains (Kim et al., 2012) and 3D shaped grains (Kim and Yoon, 2013). In the works, analyses were carried out by an explicit time integration scheme and it opened the possibility that the necking behavior is able to be predicted from CPFEM. However, the necking shape and load–displacement curve were not predicted. In this study, for an accurate prediction of necking and load–displacement curve, analyses were carried out with an implicit time integration scheme and more reasonable load–displacement curve could be obtained. Moreover, experiments were carried out and were compared with the analysis results. Finally, four different damage models with coefficient calibration were newly proposed, and a model which best describes the necking behavior is proposed.

The major study points in the present work can be summarized as follows:

- Crystal plasticity finite element method is implemented for the analysis of a tensile test via VUMAT in ABAQUS/Explicit.
- Stress concentration near grain boundaries from orientation mismatch is investigated.
- Several damage models are proposed with the functions of critical shear strain, maximum shear strain, effective strain, and principal strain.
- Void initiation, growth, and coalescence behaviors are predicted using CPFEM (Crystal Plasticity FEM) and damage models.
- Necking behavior of AA 6022-T4 is analyzed using three-dimensional grain shapes and, then the results are compared to experimental results.

2. Review of crystal plasticity model

Crystal plasticity model accounts for the material deformation by crystallographic slip and for the reorientation of the crystal lattice. In this work, a Taylor–Bishop–Hill (TBH) model, which was well described by Dao and Asaro (1996), is employed. Yoon et al. (2005) implemented the TBH model into CPFEM and developed the stress update algorithm. The work has been used in this study as the engine of CPFEM and the theory is briefly described. In this study, the rate-dependent equation in the work of Yoon et al. (2005) is replaced by the rate-independent constitutive relation by ignoring the strain-rate sensitivity term. The main purpose of this work is to investigate necking behavior combined with various damage models under the framework of CPFEM.

The deformation gradient (\mathbf{F}) is decomposed into a plastic deformation (\mathbf{F}^P) and a combination of elastic deformation and rigid body motion of the crystal lattice (\mathbf{F}^e) as shown in Fig. 1, i.e.,

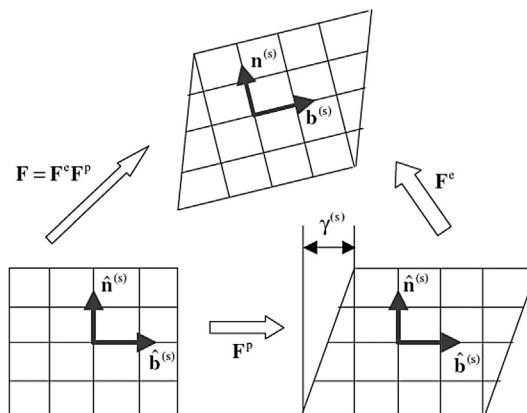


Fig. 1. Multiplicative decomposition of deformation gradient.

$$\mathbf{F} = \mathbf{F}^e \mathbf{F}^p. \quad (1)$$

Equation (1) leads to the decomposition of the velocity gradient (\mathbf{L}), into elastic and plastic parts as

$$\mathbf{L} = \mathbf{L}^e + \mathbf{L}^p. \quad (2)$$

Since the plastic deformation is assumed to be due to dislocation slip, the plastic part of velocity gradient (\mathbf{L}^p) is determined by the summation of the shear strain contribution over the entire slip systems (Dao and Asaro, 1996), as

$$\mathbf{L}^p = \sum_{(s)} \dot{\gamma}^{(s)} \mathbf{b}^{(s)} \mathbf{n}^{(s)} \quad (3)$$

Here, (s) means a slip system, and $\mathbf{n}^{(s)}$ and $\mathbf{b}^{(s)}$ are the normal to the slip plane and the vector in the slip direction, respectively. The symmetric (\mathbf{D}^p) and skew symmetric (\mathbf{W}^p) parts of the plastic velocity gradient can be written as:

$$\mathbf{D}^p = \frac{1}{2} (\mathbf{L}^p + \mathbf{L}^{pT}) = \sum_{(s)} \dot{\gamma}^{(s)} \frac{1}{2} (\mathbf{b}^{(s)} \mathbf{n}^{(s)} + \mathbf{n}^{(s)} \mathbf{b}^{(s)}) = \sum_{s=1}^N \dot{\gamma}^{(s)} \mathbf{P}_{(s)}, \quad (4)$$

$$\mathbf{W}^p = \frac{1}{2} (\mathbf{L}^p - \mathbf{L}^{pT}) = \sum_{(s)} \dot{\gamma}^{(s)} \frac{1}{2} (\mathbf{b}^{(s)} \mathbf{n}^{(s)} - \mathbf{n}^{(s)} \mathbf{b}^{(s)}) = \sum_{s=1}^N \dot{\gamma}^{(s)} \mathbf{W}_{(s)}. \quad (5)$$

It is assumed that the stress arise from the elastic distortion of the crystal lattice and that the stress–strain relation can be found through a strain energy function ϕ . To ensure objectivity of the formulation, the relation between stress and strain is based on the crystal lattice in the reference configuration. In this configuration, the second Piola–Kirchhoff stress, \mathbf{T} and its rate are determined in terms of the elastic part of the Lagrangian strain of the crystal lattice,

$$\mathbf{E}^e = \frac{1}{2} (\mathbf{F}^{eT} \cdot \mathbf{F}^e - \mathbf{I}) \quad (6)$$

$$\mathbf{T} = \frac{\partial \phi}{\partial \mathbf{E}^e} \quad \text{and} \quad \dot{\mathbf{T}} = \frac{\partial^2 \phi}{\partial \mathbf{E}^{e2}} : \dot{\mathbf{E}}^e \quad (7)$$

Since the Cauchy or true stress $\boldsymbol{\sigma}$ is used for the UMAT, it is desirable to formulate the constitutive relations in terms of Cauchy stress. However, by ignoring the contribution of the elastic volume change, the Cauchy stress is approximately equal to Kirchhoff stress, $\boldsymbol{\tau}$. They are related by $\boldsymbol{\tau} = \mathbf{J} \boldsymbol{\sigma}$, where \mathbf{J} is the determinant of \mathbf{F}^e . Constructing the constitutive relations in terms of the Kirchhoff stress rather than the Cauchy stress simplifies the formulation by eliminating the small volume strain contribution while not affecting the stress values or equilibrium noticeably.

The second Piola–Kirchhoff stress is related to the Kirchhoff stress $\boldsymbol{\tau}$, through the elastic distortion and rotation of the crystal lattice:

$$\boldsymbol{\tau} = \mathbf{F}^e \cdot \mathbf{T} \cdot \mathbf{F}^{eT} \quad (8)$$

The Kirchhoff stress rate is given by

$$\dot{\boldsymbol{\tau}} = \mathbf{F}^e \cdot \dot{\mathbf{T}} \cdot \mathbf{F}^{eT} + \dot{\mathbf{F}}^e \cdot (\mathbf{F}^{e-1} \cdot \mathbf{F}^e) \cdot \mathbf{T} \cdot \mathbf{F}^{eT} + \mathbf{F}^e \cdot \mathbf{T} \cdot (\mathbf{F}^{eT} \cdot \mathbf{F}^{e-T}) \cdot \mathbf{F}^{eT} \quad (9)$$

Recognizing that $\dot{\mathbf{E}}^e = \mathbf{F}^{eT} \cdot \mathbf{D}^e \cdot \mathbf{F}^e$, using $\dot{\mathbf{T}} = \frac{\partial^2 \phi}{\partial \mathbf{E}^{e2}} : \dot{\mathbf{E}}^e$ and substituting $\mathbf{L}^e = \mathbf{D}^e + \mathbf{W}^e$, the Kirchhoff stress rate becomes

$$\dot{\boldsymbol{\tau}} = \mathbf{F}^e \cdot \left[\frac{\partial^2 \phi}{\partial \mathbf{E}^{e2}} : (\mathbf{F}^{eT} \cdot \mathbf{D}^e \cdot \mathbf{F}^e) \right] \cdot \mathbf{F}^{eT} + \mathbf{D}^e \cdot \boldsymbol{\tau} + \boldsymbol{\tau} \cdot \mathbf{D}^e + \mathbf{W}^e \cdot \boldsymbol{\tau} - \boldsymbol{\tau} \cdot \mathbf{W}^e \quad (10)$$

The first three terms can be combined into a fourth order modulus, \mathbf{K} , and the elastic spin can be written in terms of the total spin and the plastic spin. This permits a representation in terms of the Jaumann rate of Kirchhoff stress:

$$\tilde{\boldsymbol{\tau}} = \dot{\boldsymbol{\tau}} - \mathbf{W} \cdot \boldsymbol{\tau} + \boldsymbol{\tau} \cdot \mathbf{W} = \mathbf{K} : \mathbf{D}^e - \mathbf{W}^p \cdot \boldsymbol{\tau} + \boldsymbol{\tau} \cdot \mathbf{W}^p \quad (11)$$

Writing the rate of deformation tensor as the sum of the elastic and plastic parts, the Jaumann stress rate can be expressed in terms of the total deformation rate and the plastic part.

$$\dot{\tau} = \mathbf{K} : \mathbf{D} - [\mathbf{K} : \mathbf{D}^P + \mathbf{W}^P \cdot \tau - \tau \cdot \mathbf{W}^P] \quad (12)$$

The terms in brackets on the right hand side are a function of the modulus, stress, crystal geometry and slip rate quantities. Express by using these explicitly in terms of the slip rate, the stress rate becomes

$$\dot{\tau} = \mathbf{K} : \mathbf{D} - \sum_{s=1}^N \dot{\gamma}^{(s)} [\mathbf{K} : \mathbf{P}_{(s)} + \mathbf{W}_{(s)} \cdot \tau - \tau \cdot \mathbf{W}_{(s)}] = \mathbf{K} : \mathbf{D} - \sum_{s=1}^N \dot{\gamma}^{(s)} \mathbf{R}_{(s)} \quad (13)$$

where $\mathbf{R}_{(s)} = \mathbf{K} : \mathbf{P}_{(s)} + \mathbf{W}_{(s)} \cdot \tau - \tau \cdot \mathbf{W}_{(s)}$ is a rotation tensor that depends on the slip plane normal and direction, stress, and elastic modulus. Equation (13) is used to update the stress at the integration point after the unknowns $\dot{\gamma}^{(s)}$ are solved at the slip system level. Then, the grain level stress at $t + \Delta t$ is updated as

$$\tau_{(n+1)} = \mathbf{R}\tau_{(n)}\mathbf{R}^T + \Delta t \dot{\tau}, \quad (14)$$

where \mathbf{R} is the pure rotation tensor of materials, which is obtained by the polar decomposition. The determination process of the unknowns $\dot{\gamma}^{(s)}$ is described in detail in the work of Yoon et al. (2005). The determination process of $\dot{\gamma}^{(s)}$ considering damage evolution is explained in Section 3.2.

3. Damage evolution models

3.1. Damage evolution models

Various damage models have been proposed by many researchers to analyze the fracture behavior of metals (Gurson, 1975; Tvergaard, 1982; Tvergaard and Needleman, 1984; Cockcroft and Latham, 1968; Johnson and Cook, 1985; Basaran and Lin, 2008; Wierzbicki et al., 2005; Beese et al., 2010; Xue, 2009; Zhang et al., 2000; Wilkins et al., 1980; Stoughton and Yoon, 2010). Cockcroft and Latham (1968) proposed a damage model with the function of the principal stress and effective strain. Johnson and Cook (1985) defined the critical equivalent fracture strain as a monotonic function of the stress triaxiality. Wierzbicki et al. (2005) assumed that fracture occurs when the accumulated equivalent plastic strain, modified by the function of the stress triaxiality and the deviatoric state parameter, reaches a critical value. Wierzbicki et al. (2005) also intensively reviewed the prediction capability of various damage models by comparing those predictions with their own experimental results. Recently, Xue (2009) and Stoughton and Yoon (2010) proposed a stress based fracture and necking criterion. These damage or fracture models were successfully employed in the prediction of fractures in the sheet metal forming process (Stoughton and Yoon, 2010), in a tensile test of a round bar and a flat plate (Nielsen and Tvergaard, 2009; Xue, 2009), and in a high velocity penetration of a long rod into an oblique plate (Liden et al., 2012).

As mentioned in section 1, the damage studies can be classified into two main approaches. In this study, we considered that the metal damage is caused by a simple criterion such as maximum shear strain, principal strain, equivalent plastic strain, and strain energy. Four simple damage models, therefore, are proposed as a function of shear strain, principal strain, equivalent plastic strain, and strain energy, respectively. All of these models belong to CDM framework and the damage is assumed to be isotropic. Many studies showed that the damage evolves anisotropically (Ekh et al., 2004; Hammi and Horstemeyer, 2007; Zairi et al., 2011; Mengonia and Ponthot, 2014). The anisotropic damage model can give more accurate results. In this study, the focus is given to predict a general necking shape under uniaxial tension for the rolling direction using simplified isotropic damage models. Anisotropic effect is indirectly considered through crystal plasticity model (not through a damage model).

1) Principal plastic strain damage model

This model defines the damage as initiated and accumulated when *principal* plastic strain is greater than a certain critical value. This model is written as

$$D = \begin{cases} 0 & (\varepsilon_1 \leq \varepsilon_{1f,ini}) \\ \frac{D_{max}}{(\varepsilon_{1f,max} - \varepsilon_{1f,ini})^M} (\varepsilon_1 - \varepsilon_{1f,ini})^M & (\varepsilon_{1f,ini} < \varepsilon_1 < \varepsilon_{1f,max}) \\ D_{max} & (\varepsilon_{1f,max} \leq \varepsilon_1) \end{cases} \quad (15)$$

In Equation (15), ε_1 is the principal plastic strain, $\varepsilon_{1f,ini}$ is the principal plastic strain over which damage initiates, $\varepsilon_{1f,max} = \varepsilon_{1f,ini} + \Delta \varepsilon_{1f}$ is the maximum principal plastic strain at which the damage value reaches the maximum

value D_{max} , and M is the exponent to control the damage evolution order. Fig. 2 shows a schematic illustration of the damage value and flow stress relaxation for the exponent of M . When the exponent M is 1.0, the flow stress changes abruptly if the equivalent plastic strain reaches $\epsilon_{1f,ini}$ and decreases linearly with the equivalent plastic strain. This abrupt change of flow stress sometimes causes a convergence problem in a static implicit analysis. In this study, therefore, the exponent M is set to 2.0 in order to make smoother the change of the flow stress and to improve convergence.

2) Equivalent plastic strain damage model

This model defines the damage as initiated and accumulated when *equivalent* plastic strain is greater than a certain critical value. This model is written as

$$D = \begin{cases} 0 & (\bar{\epsilon} \leq \bar{\epsilon}_{f,ini}) \\ \frac{D_{max}}{(\bar{\epsilon}_{f,max} - \bar{\epsilon}_{f,ini})^M} (\bar{\epsilon} - \bar{\epsilon}_{f,ini})^M & (\bar{\epsilon}_{f,ini} < \bar{\epsilon} < \bar{\epsilon}_{f,max}) \\ D_{max} & (\bar{\epsilon}_{f,max} \leq \bar{\epsilon}) \end{cases} \quad (16)$$

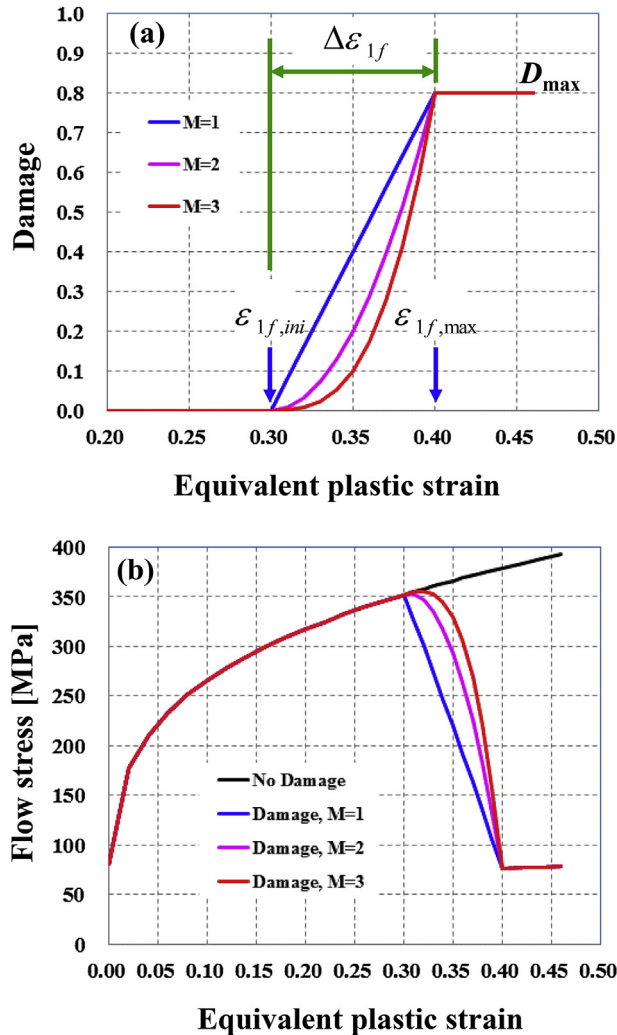


Fig. 2. Schematic illustration of damage evolution.

In Equation (16), D is damage, D_{\max} is the maximum damage value, $\bar{\epsilon}$ is the equivalent plastic strain, $\bar{\epsilon}_{f,ini}$ is the equivalent plastic strain over which damage initiates, $\bar{\epsilon}_{f,max} = \bar{\epsilon}_{f,ini} + \Delta\bar{\epsilon}_f$ is the maximum equivalent plastic strain at which the damage value reaches the maximum value D_{\max} , and M is the exponent that has the same meaning as the exponent in the principal plastic strain damage model.

3) Maximum shear strain damage model

This model defines the damage as initiated and accumulated when *maximum shear strain* is greater than a certain critical value. This model is written as

$$D = \begin{cases} 0 & (\gamma_m \leq \gamma_{mf,ini}) \\ \frac{D_{\max}}{(\gamma_{mf,max} - \gamma_{mf,ini})^M} (\gamma_m - \gamma_{mf,ini})^M & (\gamma_{mf,ini} < \gamma_m < \gamma_{mf,max}) \\ D_{\max} & (\gamma_{mf,max} \leq \gamma_m) \end{cases} \quad (17)$$

In Equation (17), γ_m is the maximum shear strain, $\gamma_{mf,ini}$ is the maximum shear strain over which damage initiates, $\gamma_{mf,max} = \gamma_{mf,ini} + \Delta\gamma_{mf}$ is the maximum shear strain at which the damage value reaches the maximum value D_{\max} , and M is the exponent that has the same meaning as that of the principal plastic strain damage model.

4) Strain energy damage model

This model defines the damage as initiated and accumulated when the equivalent stress is greater than a certain critical value. In this model, damage is accumulated by means of strain energy. This model is written as

$$dD = \begin{cases} 0 & (\bar{\sigma} \leq \bar{\sigma}_{f,ini}) \\ \frac{\bar{\sigma}}{\bar{\sigma}_{f,ini}(\bar{\epsilon}_{f,max} - \bar{\epsilon}_{f,ini})} d\bar{\epsilon} & (\bar{\sigma}_{f,ini} < \bar{\sigma} \text{ and } D < D_{\max}) \\ 0 & (D_{\max} \leq D) \end{cases} \quad (18)$$

$$D = \int dD \quad (19)$$

In Equation (18), $\bar{\sigma}$ is the equivalent stress, $\bar{\sigma}_{f,ini}$ is the initial critical equivalent stress over which damage initiates, $\bar{\epsilon}$ is the equivalent plastic strain, and $\bar{\epsilon}_{f,max} - \bar{\epsilon}_{f,ini} = \Delta\bar{\epsilon}_f$ is the strain increment from damage initiation to maximum damage.

3.2. Numerical implementation of damage evolution

As damage accumulates, the load carrying capacity of the materials decreases. To consider the decrease of load carrying capacity, the flow stress of the materials is downscaled with the calculated damage as (Lemaitre et al., 2000; Lemaitre and Desmorat, 2005; Xue, 2007)

$$\bar{\sigma}_D(\bar{\epsilon}, D) = (1 - D)\bar{\sigma}(\bar{\epsilon}). \quad (20)$$

In Equation (20), $\bar{\sigma}(\bar{\epsilon})$ is the flow stress calculated using the equivalent plastic strain and $\bar{\sigma}_D(\bar{\epsilon}, D)$ is the modified flow stress considering the damage evolution. In this study, it is assumed that the damage and strain hardening are isotropic. By assuming a simple isotropic damage evolution, the damage value is calculated in an integration point level and applied to slip system-wise by solving the nonlinear Equation (23) and damage is accumulated in an explicit way as follows.

(i) Calculate the trial stress.

The trial stress at the slip system level by assuming fully elastic deformation is calculated by Yoon et al. (2005)

$$\tau_{(n+1)}^{T(s)} = \tau_{(n)}^{(s)} + \Delta t \dot{\tau}^{(s)} = \tau_{(n)}^{(s)} + \Delta t \mathbf{R}_{(s)} : \mathbf{D} \quad (21)$$

In Equation (21), $\tau_{(n+1)}^{T(s)}$ is the trial resolved shear stress at the current step, $\tau_{(n)}^{(s)}$ is the resolved shear stress at the previous step calculated from Equation (26) considering the softening by damage, $\mathbf{R}_{(s)}$ is defined in Equation (13).

The resolved shear stress $\tau^{(s)}$ also follows the rate-dependent hardening rule

$$\tau^{(s)} = g^0 \left(\frac{|\dot{\gamma}^{(s)}|}{\dot{\gamma}_0} \right)^m \text{sign}(\dot{\gamma}^{(s)}) \quad (22)$$

where $g^0 = a(\epsilon_0 + I)^n$ is a static part of hardening in a grain level. I is the accumulated slip on all the slip system and it is expressed as $I = I_n + \dot{I}\Delta t$ where $\dot{I} = \sum \dot{\gamma}^{(s)}$. m is the strain-rate sensitivity exponent. The exponent m is assumed to be zero in this study for rate-independent behavior of materials.

(ii) Calculate plastic strain rate $\dot{\gamma}^{(s)}$ by solving following nonlinear equation.

When the materials deforms plastically, the slip system stress in Eq. (21) must be equal to the resolve shear stress in Eq. (22). By solving the following nonlinear equation, i.e., Yoon et al. (2005).

$$F(\dot{\gamma}^{(s)}) = \tau_{(n+1)}^{T(s)} - \Delta t \sum_{\alpha} \dot{\gamma}^{(\alpha)} \mathbf{R}_{(s)} : \mathbf{P}_{(\alpha)} - (1 - D_{(n)})\tau^{(s)} = 0 \quad (23)$$

In Equation (23), $D_{(n)}$ is the damage at the previous step, To consider the softening by damage, the flow stress is down-scaled and this is different from the work of Yoon et al. (2005). During the iteration procedure at each step, $D_{(n)}$ is not updated for better convergence purpose and is only updated after achieving the convergence at the end of each time step.

(iii) Calculate the damage increment and updated stress by

$$\Delta D_{(n+1)} = \int_{t_n}^{t_{n+1}} dD \quad (24)$$

$$D_{(n+1)} = D_{(n)} + \Delta D_{(n+1)} \quad (25)$$

$$\tau_{(n+1)}^{(s)} = (1 - \Delta D_{(n+1)}) \left(\tau_{(n+1)}^{T(s)} - \Delta t \sum_{\alpha} \dot{\gamma}^{(\alpha)} \mathbf{R}_{(s)} : \mathbf{P}_{(\alpha)} \right) \quad (26)$$

In Equations (24)–(26), ΔD_{n+1} is the damage increment calculated in an integration point level and $\tau_{(n+1)}^{(s)}$ is the updated slip system stress at the current step. Because the stress softening by damage is accumulated by Equation (26), the damage increment $\Delta D_{(n+1)}$ is used instead of total damage $D_{(n+1)}$ in Equation (26).

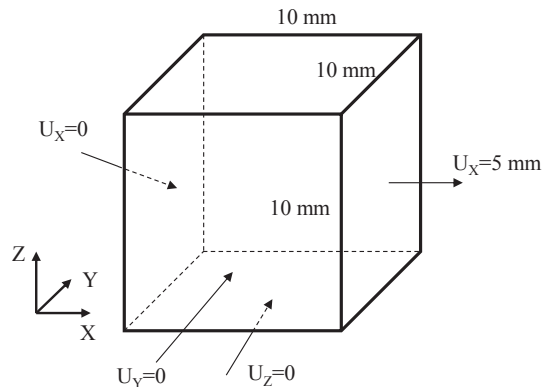


Fig. 3. Example of single element analysis for verification.

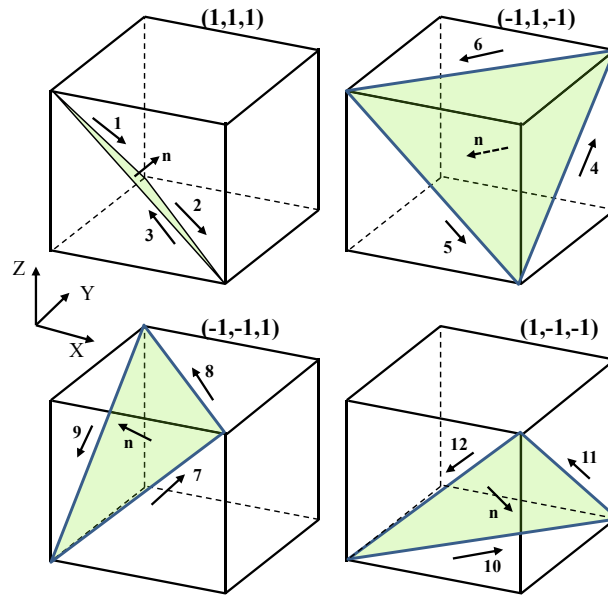


Fig. 4. Slip system definition for FCC materials.

3.3. Implementation verification

In order to verify the stress integration procedure and damage evolution model, analyses were carried out with one element. Fig. 3 shows the example for verification. The domain is discretized by a single element. Analyses were carried out

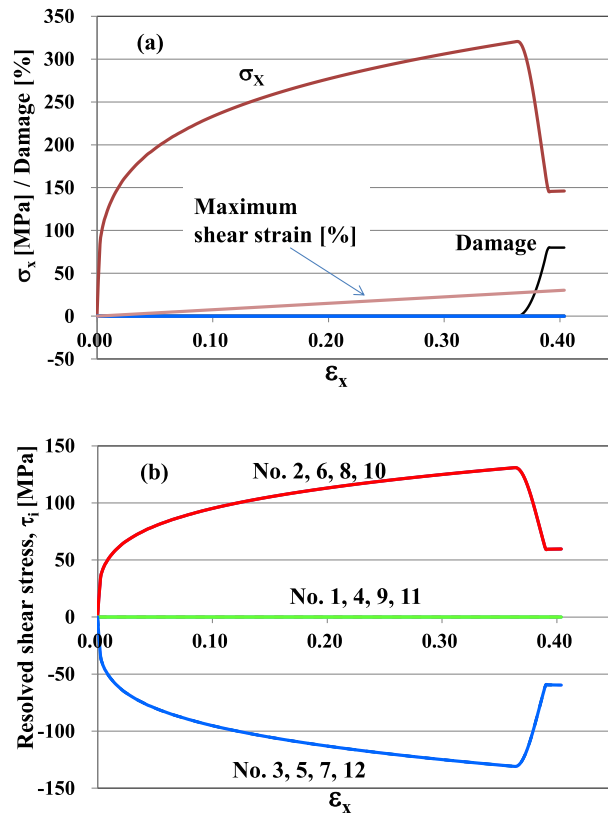


Fig. 5. Analysis results for $(0^\circ, 0^\circ, 0^\circ)$ Euler angles.

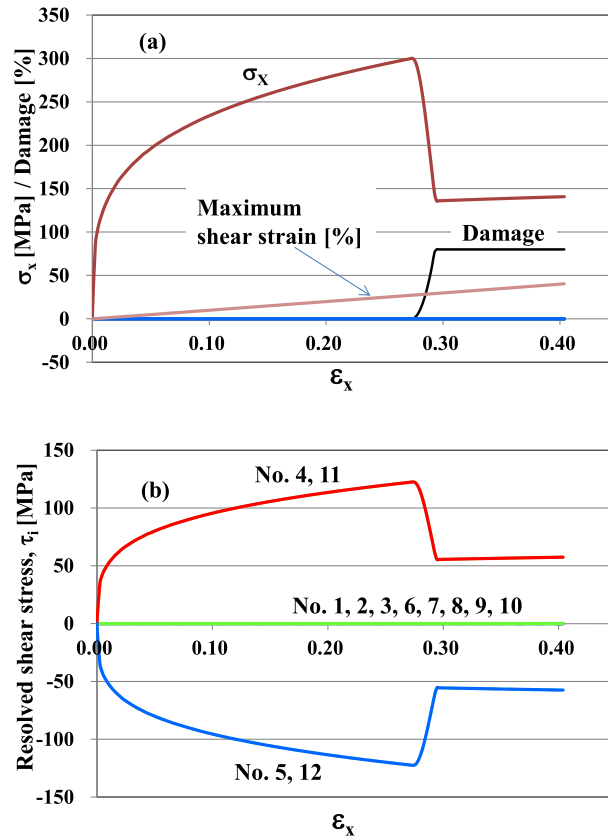


Fig. 6. Analysis results for $(45^\circ, 0^\circ, 0^\circ)$ Euler angles.

for two sets of Euler angles $(0^\circ, 0^\circ, 0^\circ)$ and $(45^\circ, 0^\circ, 0^\circ)$. 12 slip systems for FCC metals are shown in Fig. 4. The maximum shear strain damage model is used for verification. 0.272 and 0.02 are used for $\gamma_{mf,ini}/2$ and $\Delta\gamma_{mf}/2$, respectively. For the slip system hardening, Equation (28) is used and this will be explained in Section 4.2. Fig. 5 shows the analysis results for Euler angles of $(0^\circ, 0^\circ, 0^\circ)$. For stable convergence, the maximum damage is limited to 0.8. Damage starts to accumulate when the maximum shear strain is 27.2%. As damage accumulates, the longitudinal stress, σ_x , decreases due to the damage softening. Fig. 5(b) shows the resolved shear stresses along the slip systems. The slip system numbers 1, 4, 7, and 11 are normal to tensile direction, and therefore the stress is zero. The product of slip plane normal and slip direction for slip system numbers 2, 6, 8, and 10 are positive, and slip direction is at 45° angle with loading axis. Therefore, the resolved shear stress is positive. For the slip system numbers 3, 5, 7, and 12, the resolved shear stress is negative because the product of slip plane normal and slip direction is negative. Fig. 6 shows the analysis results for Euler angles of $(45^\circ, 0^\circ, 0^\circ)$. In this case, the crystal is rotated 45° around z-axis, and therefore, the slip systems which are shown in Fig. 4 are also rotated. By 45° rotation of crystal structure, the slip system numbers 1, 2, 3, 6, 7, 8, 9, and 10 become normal or parallel to the loading direction, and therefore, the resolved shear stresses are zero. With the same way with Fig. 5(b), the resolved shear stress for the slip systems of 4 and 11 are positive, and vice versa for the slip systems 5 and 12. Due to the anisotropy of the crystal structure, the maximum shear strain curve in Fig. 5(b) is different from that of Fig. 6(b). Therefore, the longitudinal strains at which damage starts are different in two cases. However, damage starts to accumulate when the maximum shear strain is 0.272 in the both cases. From these two verification examples, it is shown that the stress integration with damage evolution is well implemented.

4. Analysis model description

4.1. Finite element model for a tensile test

To predict the necking behavior of AA 6022-T4 aluminum alloy sheet, finite element analysis for a tensile test was carried out with CPFEM. The crystal plasticity and damage models described in the previous section were implemented into UMAT (User MATERIAL interface) in a commercial software of ABAQUS. For analyzing the stress concentration from the orientation mismatch, the element size should be smaller than a grain size. A great number of elements are needed for the whole tensile specimen. For computational effectiveness, therefore, the analysis domain is reduced, as shown in Fig. 7. The size of the

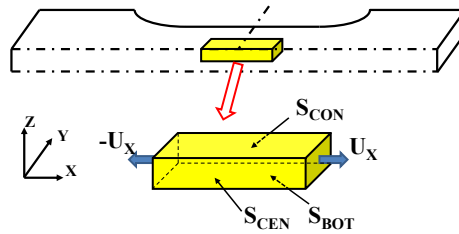


Fig. 7. Definition of analysis domain and boundary conditions for tensile test.

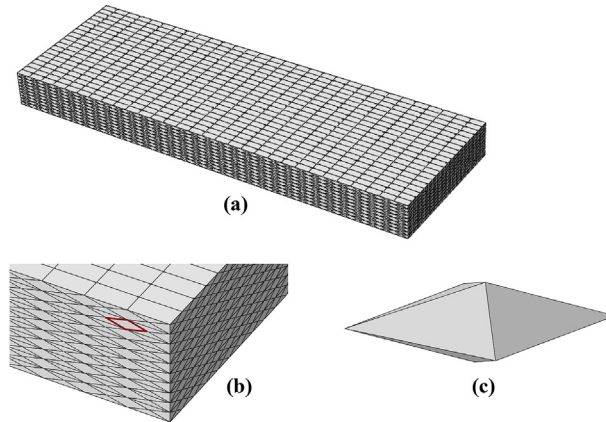


Fig. 8. Division of specimen by octagon grains: (a) full model, (b) magnified view and (c) octahedron shape of grain.

selected analysis domain is 6.0 mm in length, 2.0 mm in width, and 0.5 mm in thickness. Sheet thickness is assumed to be 1.0 mm and a half thickness is chosen considering symmetry. Tensile displacement boundary conditions are imposed for the left and right faces in the x-direction. For the front (S_{CEN}) and bottom (S_{BOT}) faces of the selected domain, the symmetric displacement conditions are imposed. For the rear face (S_{CON}), y-displacement of all the nodes is coupled to move together considering the continuity conditions in the reduced region.

Fig. 8 shows the division of the analysis domain into octagon grains. Grain shape is assumed to be a regular octahedron as shown in Fig. 8(c). Considering the shape change during the rolling process, a grain size is assumed to be about 0.2, 0.1, and 0.05 mm in x, y, and z directions, respectively. Though an average grain size of AA 6022-T4 is about 0.05 mm (Yoon et al., 2005), the sizes of grain in the rolling and transverse directions are magnified for the computational effectiveness. Each grain is discretized into sufficient number of elements and the same Euler angles are allocated to all the elements in each grain. The contours of ' $\sin \varphi \cdot \sin \phi_2$ ' (see Fig. 9(a)) show that the same orientation angles are allocated to all elements in each grain. Here, φ and ϕ_2 are the second and third Euler angles. Fig. 9(b) shows the detailed finite element discretization and ' $\sin \varphi \cdot \sin \phi_2$ ' contour for several grains. Pole figures of AA 6022-T4, shown in Fig. 10, were measured using standard X-ray diffraction techniques and orientation imaging microscopy (OIM) (Yoon et al., 2005).

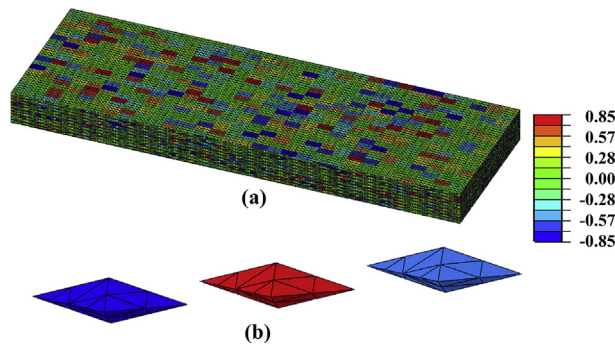


Fig. 9. Finite element discretization and contour of ' $\sin \varphi \cdot \sin \phi_2$ ' showing the correct allocation of the same orientation angles for the elements in each grain: (a) for whole domain, (b) for selected several grains.

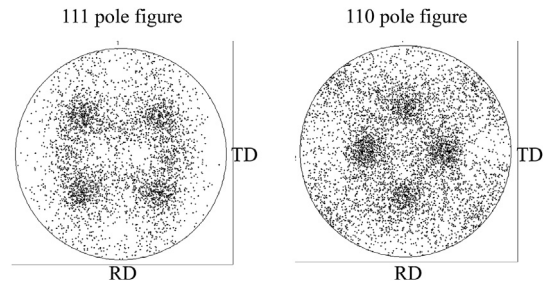


Fig. 10. (111) and (110) pole figures for aluminum 6022-T4.

4.2. Determination of slip system hardening relation

The true stress–strain relation of AA 6022-T4, obtained from tensile test along the rolling direction, is fitted with

$$\bar{\sigma}(\bar{\epsilon}) = 479.9(\bar{\epsilon} + 0.001)^{0.258} \quad (27)$$

In crystal plasticity FEM, the relation of Equation (27) is a representative relation that should be obtained from averaging the response of each slip system. A stress–strain relation at a grain level, therefore, is different from the relation represented by Equation (27). In this study, it is assumed that the grain hardening has the same form as that shown in Equation (27). Through trial and error analyses, the static part of stress–strain relation in a grain level to match Equation (27) is determined as

$$g^o = a(\epsilon_o + \Gamma)^n = 179.5(0.001 + \Gamma)^{0.240}. \quad (28)$$

Fig. 11 provides a comparison of the stress–strain relation obtained by CPFEM using the grain-level hardening of Equation (28) with that of the experimental results of Equation (27). The curve obtained from CPFEM is in good agreement with the measured curve.

5. Analysis of necking behavior

5.1. Damage initiation and evolution

Fig. 12 shows the effective stress contours at several time steps. For the results shown in Figs. 12–15, the principal strain damage model is used; ϵ_g is the gage strain calculated from the initial length (L_0) and tensile displacement (u) as $\epsilon_g = \ln((L_0 + u)/L_0)$. Determination of the damage parameters for each model is described in the next section. As expected, stress concentration takes place at many spots near the grain boundary. The stress concentration near the grain boundaries for the selected grains is shown in Fig. 13. This stress concentration is considered to be caused by the orientation mismatches between the neighboring grains. As tensile strain increases, as shown in Fig. 12(b)–(c), the stress concentration region

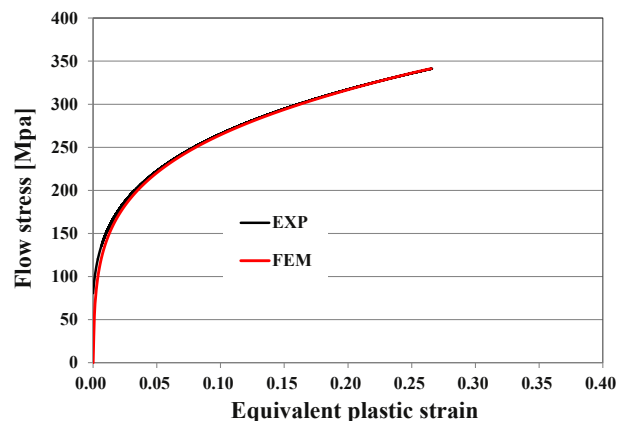


Fig. 11. Measured and analyzed flow stresses.

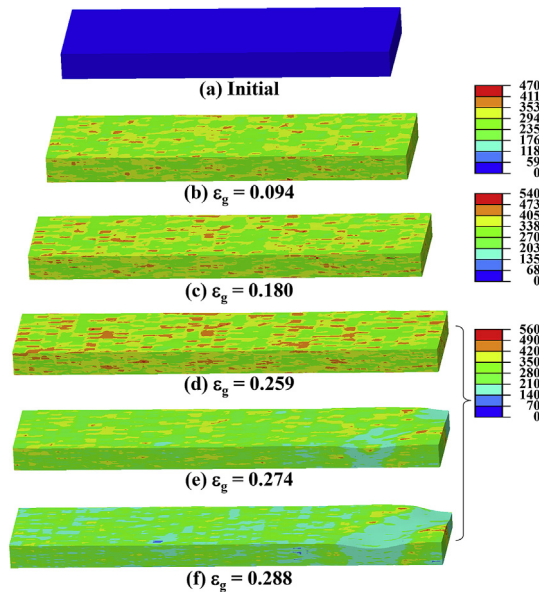


Fig. 12. Effective stress distribution (principal strain damage model, $\epsilon_{1f,ini} = 0.262$, $\epsilon_{1f,max} = 0.362$, $D_{max} = 0.8$, $M = 2$).

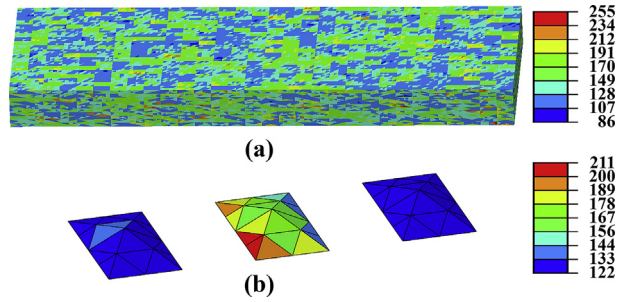


Fig. 13. Detailed view of effective stress distribution for (a) full model and (b) several grains (principal strain damage model, $\epsilon_g = 0.01$, $\epsilon_{1f,ini} = 0.262$, $\epsilon_{1f,max} = 0.362$, $D_{max} = 0.8$, $M = 2$).

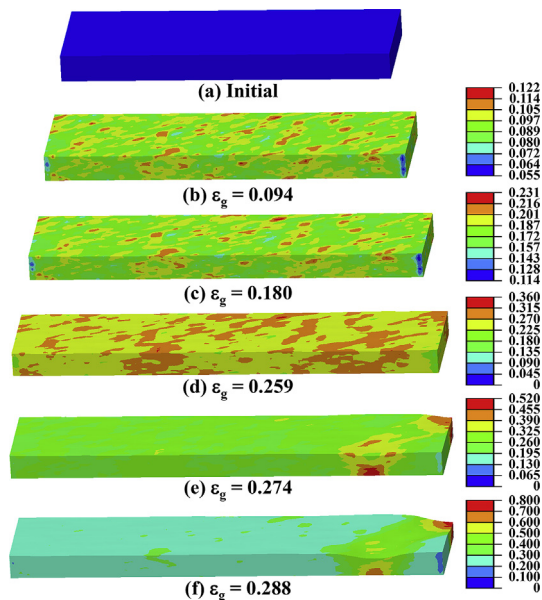


Fig. 14. Principal strain distribution (principal strain damage model, $\epsilon_{1f,ini} = 0.262$, $\epsilon_{1f,max} = 0.362$, $D_{max} = 0.8$, $M = 2$).

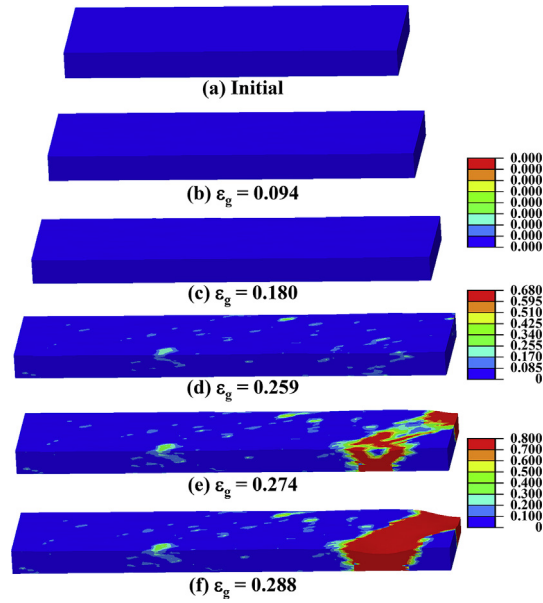


Fig. 15. Damage distribution (principal strain damage model, $\epsilon_{1f,ini} = 0.262$, $\epsilon_{1f,max} = 0.362$, $D_{max} = 0.8$, $M = 2$).

becomes larger. In Fig. 12(e) and (f), it can be seen that the stress level decreases compared to that shown in Fig. 12(d). This is because the load carrying capacity decreases due to damage initiation in the necking region. Figs. 14 and 15 show the principal strain and damage distributions for several tensile strain levels. In the same way as the equivalent stress, the concentrated principal strain is shown at many spots; the principal strain increases as the tensile strain increases, as shown in Fig. 14. When the principal strain becomes greater than a critical value ($\epsilon_{1f,ini}$), damage initiates and accumulates, and their stress levels are lowered by softening (see Fig. 12(c) and (d)). With the stress softening, the localized deformation takes place in the damaged region (see Fig. 14(e) and (f)). In Fig. 15, it can be shown that there is no damaged element when the gauge strain is less than or equal to 0.180. When the gauge strain reaches 0.259, many damaged elements are shown in the certain areas. This phenomenon is similar to void nucleation. As tensile strain increases, the damaged area increases, and lead to combine the neighboring damaged regions. These growth and combination of damaged areas are correlated to the void growth and void coalescence phenomena, respectively. Finally, most of the elements in the necking region are damaged. In the analysis, necking starts to take place when the gage strain is about 0.274. The necking strain is controlled by the parameter $\epsilon_{1f,ini}$.

In Fig. 16, the obtained longitudinal strain is compared to that from the experimental results. The strain in Fig. 16(a) is measured using the ARAMIS (Ivanov et al., 2007) system. ARAMIS is an optical deformation and strain measurement system. In the strain measurement with the ARAMIS system, droplets of sprayed particles are used as the reference points instead of regular grids; therefore, very local strain can be measured. The maximum strain, obtained by CPFEM and shown in the upper right corner of Fig. 16(b) is about 1.2; this value is much higher than the measured value of 0.58. Except for the strain in this localized region, the longitudinal strain in other regions in CPFEM is similar to that of the experiment. The deformed necking shapes just before fracture are also shown, for the comparison purpose, in Fig. 17. The length of the necking region in the

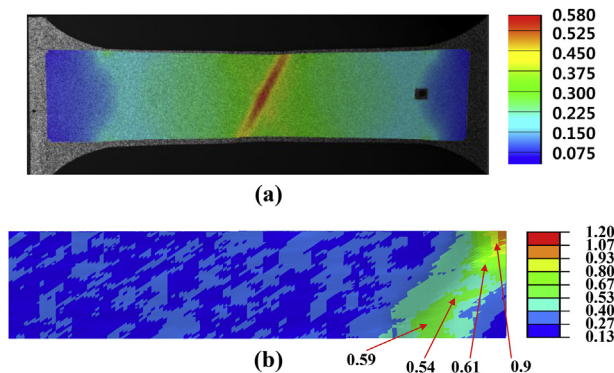


Fig. 16. Comparison of longitudinal strain obtained by (a) experiment and (b) CPFEM (principal strain damage model, $\epsilon_{1f,ini} = 0.262$, $\epsilon_{1f,max} = 0.362$, $D_{max} = 0.8$, $M = 2$).

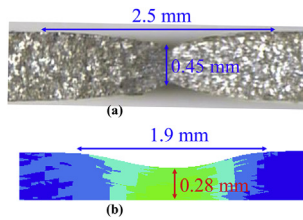


Fig. 17. Comparison of sectional deformed shape just before fracture obtained by (a) experiment and (b) CPFEM (principal strain damage model, $\epsilon_{1f,ini} = 0.262$, $\epsilon_{1f,max} = 0.362$, $D_{max} = 0.8$, $M = 2$).

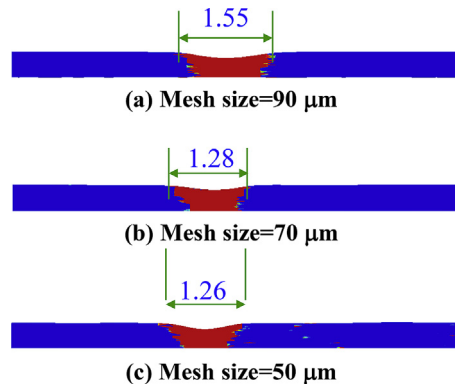


Fig. 18. Comparison of necking shape for various mesh sizes ($\epsilon_g = 0.281$).

experiment is 24% greater than that predicted from CPFEM; the thickness of the necking region just before fracture is 24% smaller than that predicted from CPFEM. Even though the predicted necking length and the minimum sheet thickness contain 24% error, it is considered that the results are reasonable.

In the analysis of necking with damage, it is known that softening is the cause of material instability and the results may depend on the mesh size (Jirasek and Bazant, 2002). A nonlocal regularization technique is usually used to overcome this instability issue (Jirasek and Bazant, 2002; Nguyen, 2005; Grassl and Jirásek, 2006; Nguyen et al., 2015). In this study, mesh dependent solutions are investigated instead of using nonlocal regularization. Analyses are carried out for various mesh sizes and reasonable mesh size is determined. Fig. 18 shows the necking shapes for various element sizes. When the element size is 90 μm , the size of necking zone is 1.55 mm. When the element size is 70 μm , the size of necking zone decreases to 1.28 mm and this is almost the same with that when element size is 50 μm . For detailed investigation, stress concentration (Von Mises stress) in an early stage of tensile test is shown in Fig. 19. When the element size is 90 μm , the peak stress is lower and the stress concentration region is wider than the case when mesh size is 70 μm . With this reason, the size of necking region is bigger as mesh size increases as shown in Fig. 18. For the experimental verification, three tensile tests were carried out and the load–displacement relations were compared in Fig. 20(a). The hardening behaviors of three cases are almost the same. The fracture displacement, however, is a little bit different. However, the difference is not so big and the first one (EXP1) is in the middle of three cases. Therefore, the first one (EXP1) is selected as the reference experiment result for comparison in this study. The load–displacement relation for various sizes of element is shown in Fig. 16(b). When the element size is 90 μm , a load–displacement curve is predicted lower than the others. For a large element, the maximum stress from stress concentration is smaller than the case of a smaller element is used as shown in Fig. 15. This is due to the lower strain hardening and therefore a lower tensile load is predicted when the element size is large. When the element size is decreased to 70 μm , the load–displacement curve goes up and is nearly the same with that of element size of 50 μm . Therefore, it is considered that a converged solution can be obtained when the element size is smaller than 70 μm .

In Figs. 18–20, it is shown that size of necking zone and the concentrated peak stress are saturated when mesh size is 50 μm . In all of the analysis in this study, therefore, mesh size is set as 50 μm .

5.2. Determination of damage model parameters

Analyses are carried out for the determination of the parameters for each damage model. Fig. 21 shows the load–displacement curves for various damage models and damage parameters. The gage length and specimen size in experiment are different from the ones of analysis. The gage lengths in experiment and analysis are 60.0 and 6.0 mm, respectively. The initial specimen areas are 25.0 and 1.0 mm^2 for experiment and analysis, respectively. For the comparison, the experimentally measured load is divided by 25.0 to make the sectional area to 1.0 mm^2 ($F_{exp,conv} = F_{exp}/25$). The conversion of experimental displacement is a little bit complex. Up to uniform deformation point, because the displacement is

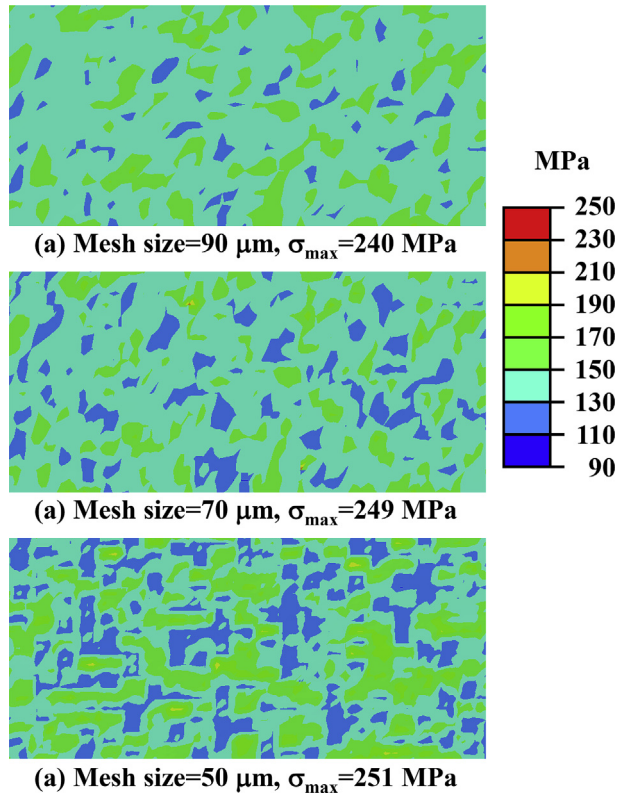


Fig. 19. Comparison of Von-mises stress distribution for various mesh sizes ($\epsilon_g = 0.01$).

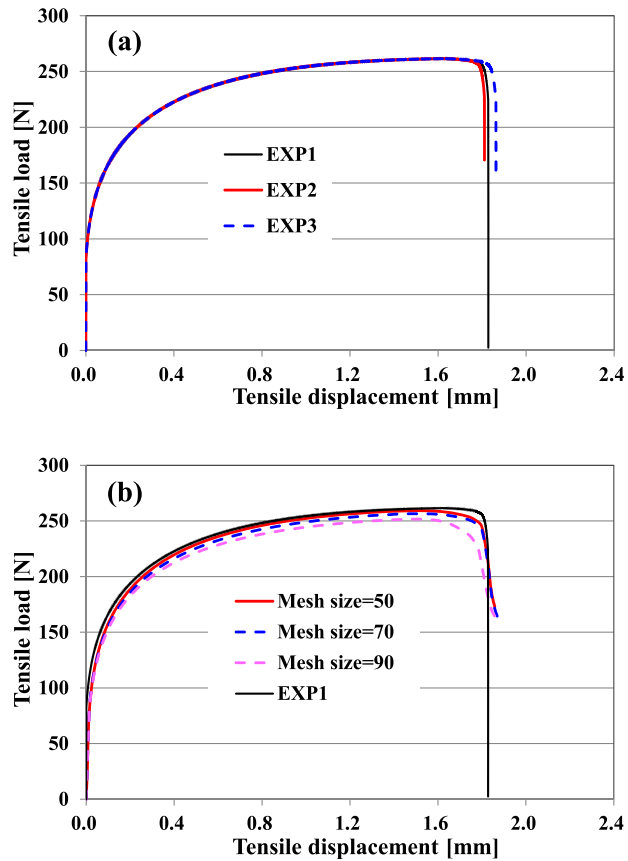


Fig. 20. Comparison of load–displacement curves for (a) three cases of experiments and (b) different element size.

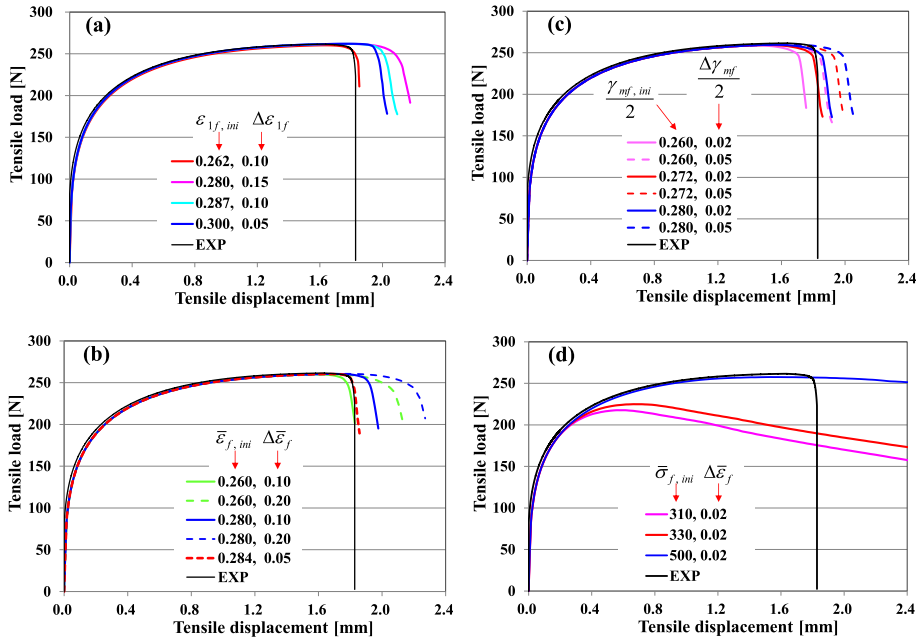


Fig. 21. Load–displacement relation for several damage parameters: (a) principal strain damage model, (b) equivalent plastic strain damage model, (c) maximum shear strain damage model, (d) equivalent strain energy damage model ($D_{max} = 0.8$, $M = 2$, gage length = 6.0 mm).

Table 1

Determined damage model parameters.

Damage model	Parameters
Principal plastic strain damage model	$\epsilon_{1f,ini} = 0.262$, $\epsilon_{1f,max} = 0.362$, $D_{max} = 0.8$, $M = 2$
Equivalent plastic strain damage model	$\bar{\epsilon}_f,ini = 0.284$, $\bar{\epsilon}_f,max = 0.334$, $D_{max} = 0.8$, $M = 2$
Maximum shear strain damage model	$\gamma_{mf,ini}/2 = 0.272$, $\gamma_{mf,max}/2 = 0.292$, $D_{max} = 0.8$, $M = 2$

proportional to strain and gage length, experimental displacement is divided by 10.0 ($u_{exp,conv} = u_{exp}/10$). After necking initiation, it is assumed that most of deformation takes place in necking region. The other regions, therefore, does not elongate anymore. Therefore, displacement after necking is regarded as the converted displacement as ($u_{exp,conv} = u_{exp,neck}/10 + (u_{exp} - u_{exp,neck})$). The converted load and displacement in this method are used for the comparison in Fig. 21.

The parameters that best fit the experimental load–displacement relation are chosen for each model and shown in Table 1. In Fig. 21(a) and (b), which showing the load–displacement relations obtained from CPFEM using the principal strain and equivalent plastic strain damage models, the experimental load–displacement relation and sudden drop of load carrying capacity after necking are well predicted by CPFEM with the determined damage parameters (solid red line in Fig. 21(a) and dotted red line (in the web version) in Fig. 21(b)). In Fig. 21(c), which shows the load–displacement relations obtained from

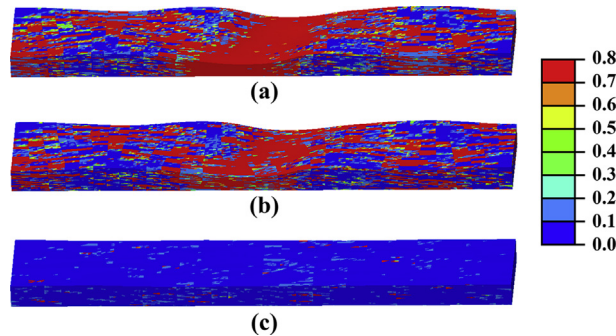


Fig. 22. Deformed shape and damage distribution for (a) $\bar{\sigma}_f,ini = 310$ MPa, (b) $\bar{\sigma}_f,ini = 330$ MPa, and (c) $\bar{\sigma}_f,ini = 500$ MPa (strain energy damage model, $\Delta\bar{\epsilon}_f = 0.02$, $D_{max} = 0.8$, $M = 2$, $\epsilon_g = 0.4$).

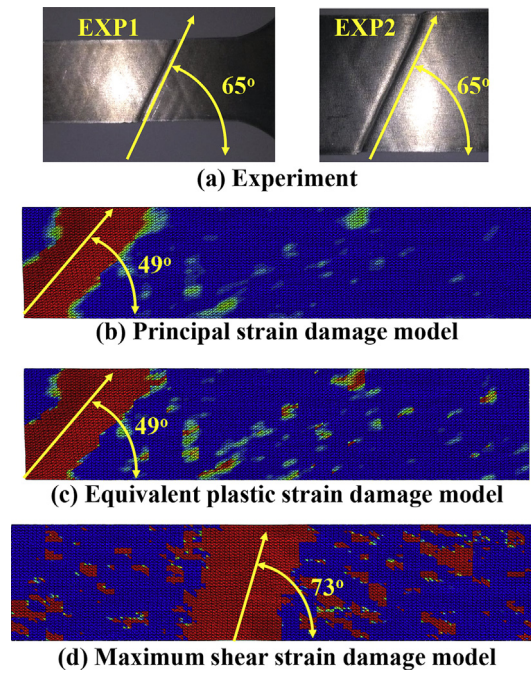


Fig. 23. Comparison of predicted necking direction with experimental result.

CPFEM using the maximum shear strain damage model, however, the load–displacement relation can be seen to contain a slight amount of error near the necking region. In this case, the best fit is determined to be the solid red line. In the strain-based damage model of Fig. 21(a)–(c), it is shown that $\varepsilon_{1f,ini}$, $\bar{\varepsilon}_{f,ini}$, and $\gamma_{mf,ini}/2$ control the initiation of necking, and $\Delta\varepsilon_{1f}$, $\Delta\bar{\varepsilon}_f$, and $\Delta\gamma_{mf}/2$ control the drop rate of load carrying capacity, i.e., the size of necking zone. As the value of $\Delta\varepsilon_{1f}$, $\Delta\bar{\varepsilon}_f$, and $\Delta\gamma_{mf}/2$ decrease, the load decrease sharply after necking. In this case the size of necking zone is small.

For the strain energy damage model shown in Fig. 21(d), the load–displacement relation up to 0.27 of the gage strain is accurately predicted when the fracture initiation equivalent stress ($\bar{\sigma}_{f,ini}$) is 500 MPa. However, the sudden drop of the load carrying capacity after necking cannot be predicted accurately. This is also shown in Fig. 22. Fig. 22 shows the deformed shapes and damage distributions for various values of damage initiation equivalent stress. When the damage initiation equivalent stress is 500 MPa, no necking is shown up to a gage strain of 0.4. Also, when the damage initiation equivalent stresses are 310 and 330 MPa (see Fig. 22(a) and (b)), no necking region is clearly shown and the thickness varies in the wide region of the sheet specimen. This phenomenon is not consistent with the experimental result, which shows quite uniform thickness except for the necking region. The load–displacement relations obtained from CPFEM for the damage initiation

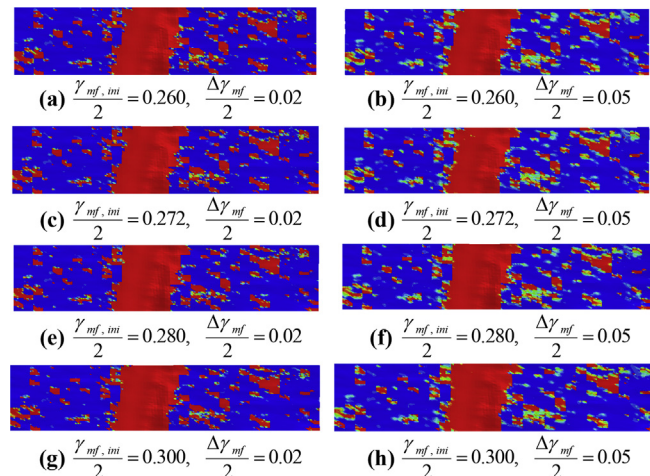


Fig. 24. Necking shapes for various damage parameters (maximum shear strain damage model).

stresses of 310 and 330 MPa up to the gauge strain of 0.27, as can be seen in Fig. 21(d), also show a large discrepancy from that of the experiment. Therefore, it is concluded that the strain energy damage model cannot predict the necking behavior of sheet metal accurately.

In Fig. 23, the predicted necking directions obtained from CPFEM for the three damage models were compared to the experimental results. The necking angle obtained in the tensile test along the rolling direction is 65° , as shown in Fig. 23(a). Two cases of experiment (EXP1 and EXP2) show the same necking angle. The predicted necking angles using the principal strain and the equivalent plastic strain damage models are the same at 49° (25% error). In the case of the maximum shear strain damage model, the necking angle is 73° (12% error). Though the necking angle is not very accurately predicted by all three of models, the prediction using CPFEM and the damage models is reasonable. The accuracy can be improved, for example, considering the real grain shapes from a micro-structure builder and grain boundary interactions.

Fig. 24 shows the necking shape for various damage parameters (maximum shear strain damage model). The necking shapes in Fig. 24 are obtained at different tensile strains for the accurate comparisons of the necking shape. The initiation of necking changes with the parameters as shown in Fig. 21. However, the necking angle almost does not change although different damage parameters are used as shown in Fig. 24. It is shown that the type of damage model has an effect on the necking angle, but the damage parameters have no effect on the necking angle.

6. Conclusion

Necking behavior of AA 6022-T4 sheet was analyzed based on a crystal plasticity model. A tensile specimen was modeled using octahedron shaped 3-dimensional grains. Each grain was discretized into many elements and the same orientations were allocated to all elements in the same grain. Stress concentration was observed at many spots due to the orientation mismatch near the grain boundaries. This stress concentration was considered to cause the damage initiation and evolution. The void nucleation, growth, and coalescence phenomena were well described by the proposed methodology. To describe the sudden drop of load carrying capacity after necking, four damage models were employed. The damage parameters for each model were determined based on the stress–strain relation obtained from tensile test. The strain-based damage models, i.e., the principal strain damage model, equivalent plastic strain damage model, and maximum shear strain damage model, accurately predicted the experimentally obtained stress–strain relation and sudden drop of load carrying capacity after necking. However, the stress based damage model, i.e., the strain energy damage model, could not accurately predict the necking behavior. The predicted necking strain, deformed shape, and necking direction were also compared to the results from the experiment. The maximum error in the predicted necking shapes, i.e., the length of the necking region and the minimum sheet thickness, was about 24%. Among the three strain-based damage models, the maximum shear strain damage model predicted the necking angle most accurately with 12% error. As a result, it was shown that the CPFEM with damage models can reasonably predict the necking behavior and necking direction without any initial imperfections.

Acknowledgments

This research was supported by a grant from the Advanced Technology Center (ATC) program (No. 10045724) funded by of Trade, Industry & Energy of Korea. This work was also partially supported by the AutoCRC program (Project code: 3-122) in Australia.

References

- ABAQUS Inc, 2012. ABAQUS Theory Manual, Version 6.12.
- Asaro, R.J., Needleman, A., 1985. Texture development and strain hardening in rate dependent polycrystals. *Acta Metall.* 33, 923–953.
- Basaran, C., Lin, M., 2008. Damage mechanics of electromigration induced failure. *Mech. Mater.* 40, 66–79.
- Beausir, B., Toth, L.S., Neale, K.W., 2007. Role of strain-rate sensitivity in the crystal plasticity of hexagonal structures. *Int. J. Plasticity* 23, 227–243.
- Beese, A.M., Luo, M., Li, Y., Bai, Y., Wierzbicki, T., 2010. Partially coupled anisotropic fracture model for aluminum sheets. *Eng. Fract. Mech.* 77, 1128–1152.
- Bettaieb, M.B., Abed-Meraim, F., 2015. Investigation of localized necking in substrate-supported metal layers: comparison of bifurcation and imperfection analyses. *Int. J. Plasticity* 65, 168–190.
- Bieler, T., Eisenlohr, P., Roters, F., Kumar, D., Mason, D.E., Crimp, M.A., Raabe, D., 2009. The role of heterogeneous deformation on damage nucleation at grain boundaries in single phase metals. *Int. J. Plasticity* 25, 1655–1683.
- Borg, U., 2007. Strain gradient crystal plasticity effects on flow localization. *Int. J. Plast.* 23, 1400–1416.
- Bridier, F., McDowell, D.L., Villechaise, P., Mendez, J., 2009. Crystal plasticity modeling of slip activity in Ti–6Al–4V under high cycle fatigue loading. *Int. J. Plasticity* 25, 1066–1082.
- Choi, S.-H., Kim, E.-Y., Kim, S.I., 2014. The micromechanical deformation behaviors of hot-rolled 590FB steel during hole-expansion test. *Int. J. Plasticity* 58, 184–200.
- Choi, S.H., Kim, D.H., Park, S.S., You, B.S., 2010. Simulation of stress concentration in Mg alloys using the crystal plasticity finite element method. *Acta Mater.* 58, 320–329.
- Choi, S.-H., Kim, E.-Y., Woo, W., Han, S.H., Kwak, J.H., 2013. The effect of crystallographic orientation on the micromechanical deformation and failure behaviors of DP980 steel during uniaxial tension. *Int. J. Plasticity* 45, 85–102.
- Cockcroft, M.G., Latham, D.J., 1968. Ductility and the workability of metals. *J. Inst. Metals* 96, 33–39.
- Dao, M., Asaro, R.J., 1996. Localized deformation modes and non-schmid effects in crystalline solids. Part I. Critical conditions of localization. *Mech. Mater.* 23, 71–102.
- Dao, M., Li, M., 2001. A micromechanical study on strain-localization-induced fracture initiation in bending using crystal plasticity models. *Phil. Mag. A* 81, 1997–2020.

- Eisenlohr, P., Diehl, M., Lebensohn, R.A., Roters, F., 2013. A spectral method solution to crystal elasto-viscoplasticity at finite strains. *Int. J. Plasticity* 46, 37–53.
- Ekh, M., Lillbacka, R., Runesson, K., 2004. A model framework for anisotropic damage coupled to crystal (visco)plasticity. *Int. J. Plasticity* 20, 2143–2159.
- Franz, G., Abed-Meriam, F., Berveillier, M., 2013. Strain localization analysis for single crystals and polycrystals : towards microstructure-ductility linkage. *Int. J. Plasticity* 48, 1–33.
- Grassl, P., Jirásek, M., 2006. Plastic model with non-local damage applied to concrete. *Int. J. Numer. Anal. Methods Geomech.* 30, 71–90.
- Gurson, A.L., 1975. *Plastic Flow and Fracture Behaviour of Ductile Materials Incorporating Void Nucleation, Growth and Coalescence* (PhD Diss). Brown University.
- Hammi, Y., Horstemeyer, M.F., 2007. A physically motivated anisotropic tensorial representation of damage with separate functions for void nucleation, growth, and coalescence. *Int. J. Plasticity* 23, 1641–1678.
- Hill, R., Hutchinson, J.W., 1975. Bifurcation phenomena in the plane tension test. *J. Mech. Phys. Solids* 23, 239–264.
- Inal, K., Neal, K.W., Aboutajeddine, 2005. Forming limit comparisons for FCC and BCC sheets. *Int. J. Plasticity* 21, 1255–1266.
- Ivanov, D., Vandenbosche, K., Ivanov, S., Baudry, K., Lomov, S., Verpoest, L., 2007. Strain mapping analysis of various textile composite and noise filtering of the data. In: *Proceedings of the OPTIMESS2007 Workshop, 28th–30th May 2007, Leuven, Belgium*.
- Jirásek, M., Bazant, Z.P., 2002. *Inelastic Analysis of Structures*. John Wiley & Sons.
- Johnson, G.R., Cook, W.H., 1985. Fracture characteristics of three metals subjected to various strains, strain rates, temperatures and pressures. *Eng. Fract. Mech.* 21, 31–48.
- Kanjarla, A.K., Houtte, P.V., Delannay, L., 2010. Assessment of plastic heterogeneity in grain interaction models using crystal plasticity finite element method. *Int. J. Plasticity* 24, 1220–1233.
- Knezevic, M., Levinson, A., Harris, R., Mishra, R.K., Doherty, R.D., Kalidindi, S.R., 2010. Deformation twinning in AZ31: influence on strain hardening and texture evolution. *Acta Mater.* 58, 6230–6242.
- Kim, H.-K., Oh, S.I., 2003. Finite element analysis of grain-by-grain deformation by crystal plasticity with couple stress. *Int. J. Plasticity* 19, 1245–1270.
- Kim, J.-B., Hong, S.-H., Yoon, J.W., 2012. Prediction of necking in tensile test using crystal plasticity model and damage model. *J. Kor. Soc. Prec. Eng.* 29, 818–823.
- Kim, J.-B., Yoon, J.W., 2013. Analysis of the necking behaviors with the crystal plasticity model using 3-dimensional shaped grains. *Adv. Mater. Res.* 684, 357–361.
- Lebensohn, R.A., Tomé, C.N., 1993. A self-consistent anisotropic approach for the simulation of plastic deformation and texture development of polycrystals: application to zirconium alloys. *Acta Metallurgica Materialia* 41, 2611–2624.
- Lemaître, J., 1985. Coupled elasto-plasticity and damage constitutive equations. *Comput. Methods Appl. Mech. Eng.* 51, 31–49.
- Lemaître, J., Chaboche, J.L., 1990. *Mechanics of Solid Materials*. Cambridge Univ. Press.
- Lemaître, J., Desmorat, R., 2005. *Engineering Damage Mechanics: Ductile, Creep, Fatigue and Brittle Failures*. Springer.
- Lemaître, J., Desmorat, R., Sauzay, M., 2000. Anisotropic damage law of evolution. *Eur. J. Mech. A/Solids* 19, 187–208.
- Li, H.W., Yang, H., Sun, Z.C., 2008. A robust integration algorithm for implementing a rate dependent crystal plasticity into explicit finite element method. *Int. J. Plasticity* 24, 267–288.
- Li, S., Houtte, P.V., Kalidindi, S.R., 2004. A quantitative evaluation of the deformation texture predictions for aluminium alloys from crystal plasticity finite element method. *Model. Simul. Mater. Sci. And Eng* 12, 845–870.
- Lidén, E., Mousavi, S., Helte, A., Lundberg, B., 2012. Deformation and fracture of a long-rod projectile induced by an oblique moving plate: numerical simulations. *Int. J. Impact. Eng.* 40–41, 35–45.
- Lin, B., Zhao, L.G., Tong, J., 2011. A crystal plasticity study of cyclic constitutive behaviour, crack-tip deformation and crack-growth path for a polycrystalline nickel-based superalloy. *Eng. Fract. Mech.* 78, 2174–2192.
- Malcher, L., Andrade Pires, F.M., Cesar de Sa, J.M.A., 2012. An assessment of isotropic damage constitutive models under high and low stress triaxialities. *Int. J. Plasticity* 30–31, 81–115.
- Malcher, L., Reis, F.J.P., Andrade Pires, F.M., Cesar de Sa, J.M.A., 2013. Evaluation of shear mechanisms and influence of the calibration point on the numerical results of the GTN model. *Int. J. Mech. Sci.* 75, 407–422.
- Malcher, L., Mamiya, E.N., 2014. An improved damage evolution law based on continuum damage mechanics and its dependence on both stress triaxiality and the third invariant. *Int. J. Plasticity* 56, 232–261.
- Marciniak, Z., Kuczynski, K., 1967. Limit strains in the process of stretch-forming sheet metal. *Int. J. Mech. Sci.* 9, 609–620.
- Mayeur, J.R., Beyerlein, I.J., Bronkhorst, C.A., Mourad, H.M., Hansen, B.L., 2013. A crystal plasticity study of heterophase interface character stability of Cu/Nb bicrystals. *Int. J. Plasticity* 48, 72–91.
- Mengoni, M., Ponthot, J.P., 2014. A generic anisotropic continuum damage model integration scheme adaptable to both ductile damage and biological damage-like situations. *Int. J. Plasticity* 66, 46–70.
- Neil, J.C., Agnew, S.R., 2009. Crystal plasticity-based forming limit prediction for non-cubic metals : application to Mg alloy AZ31B. *Int. J. Plast.* 25, 379–398.
- Nguyen, G.D., 2005. *A Thermodynamic Approach to Constitutive Modelling of Concrete Using Damage Mechanics and Plasticity Theory* (PhD dissertation). Department of Engineering Science, University of Oxford. <http://www-civil.eng.ox.ac.uk/publications/theses/giang.pdf>.
- Nguyen, G.D., Korsunsky, A.M., Belnoue, P.H., 2015. A nonlocal coupled damage-plasticity model for the analysis of ductile failure. *Int. J. Plasticity* 64, 56–75.
- Nielsen, K.L., Tvergaard, V., 2009. Effect of a shear modified Gurson model on damage development in a FSW tensile specimen. *Int. J. Solids Struct.* 46, 587–601.
- Okazawa, S., 2010. Structural bifurcation for ductile necking localization. *Int. J. Non-Linear Mech.* 45, 35–41.
- Qiao, Agnew, S.R., Wu, P.D., 2014. Modeling twinning and detwinning behaviour of Mg alloy ZK60A during monotonic and cyclic loading. *Int. J. Plasticity*. <http://dx.doi.org/10.1016/j.ijplas.2014.08.010>.
- Rossiter, J., Brahme, A., Simha, M.H., Inal, K., Mishra, R., 2010. A new crystal plasticity scheme for explicit time integration codes to simulate deformation in 3D microstructures: effects of strain path, strain rate and thermal softening on localized deformation in the aluminum alloy 5754 during simple shear. *Int. J. Plasticity* 26, 1702–1725.
- Rossiter, J., Brahme, A., Inal, K., Mishra, R., 2013. Numerical analyses of surface roughness during bending of FCC single crystals and polycrystals. *Int. J. Plasticity* 46, 82–93.
- Roters, F., Eisenlohr, P., Hantcherli, L., Tjahjanto, D.D., Bieler, T.R., Raabe, D., 2010. Overview of constitutive laws, kinematics, homogenization and multiscale methods in crystal plasticity finite-element modeling: theory, experiments, applications. *Acta Mater.* 58, 1152–1211.
- Sabnis, P.A., Forest, S., Arakere, N.K., Yastrebov, V.A., 2013. Crystal plasticity analysis of cylindrical indentation on a Ni-base single crystal superalloy. *Int. J. Plasticity* 51, 200–217. <http://dx.doi.org/10.1016/j.ijplas.2013.05.004>.
- Saito, Y., Oztop, M.S., Kysar, J.W., 2012. Wedge indentation into elastic–plastic single crystals. 2: simulations for face-centered cubic crystals. *Int. J. Plasticity* 28, 70–87.
- Segurado, J., Lebensohn, R.A., Llorca, J., Tomé, C.N., 2012. Multiscale modelling of plasticity based on embedding the viscoplastic self-consistent formulation in implicit finite elements. *Int. J. Plasticity* 28, 124–140.
- Simha, M.H., Inal, K., Worswick, J.M., 2008. Path and orientation dependence of formability in the stress- and extended stress-based forming limit curves. *J. Eng. Mater. Tech.* 130, 2003–2011.
- Stoughton, T.B., Yoon, J.W., 2010. A new approach for failure criterion for sheet metals. *Int. J. Plasticity* 27, 440–459.
- Tasan, C.C., Hoefnagels, J.P.M., Diehl, M., Yan, D., Roters, F., Raabe, D., 2014. Strain localization and damage in dual phase steels investigated by coupled in-situ deformation experiments and crystal plasticity simulations. *Int. J. Plasticity* 63, 198–210.
- Teng, X., 2008. Numerical prediction of slant fracture with continuum damage mechanics. *Eng. Fract. Mech.* 75, 2020–2041.

- Tvergaard, V., 1982. On localization in ductile materials containing spherical voids. *Int. J. Fract.* 18, 237–252.
- Tvergaard, V., Needleman, A., 1984. Analysis of the cup-cone fracture in a round tensile bar. *Acta Metall.* 32, 157–169.
- Wang, L., Eisenlohr, P., Yang, Y., Bieler, T.R., Crimp, M.A., 2010. Nucleation of paired twins at grain boundaries in titanium. *Scr. Mater.* 63, 827–830.
- Wang, H., Wu, P.D., Boyle, K.P., Neale, K.W., 2011. On crystal plasticity formability analysis for magnesium alloy sheets. *Int. J. Solids Struct.* 48, 1000–1010.
- Wang, H., Wu, P.D., Boyle, K.P., Wang, J., Tome, C.N., 2013. A crystal plasticity model for hexagonal close packed (HCP) crystals including twinning and de-twinning mechanisms. *Int. J. Plasticity* 49, 36–52.
- Wierzbicki, T., Bao, Y., Lee, Y.-W., Bai, Y., 2005. Calibration and evaluation of seven fracture models. *Int. J. Mech. Sci.* 47, 719–743.
- Wilkins, M.L., Streit, R.D., Reaugh, J.E., 1980. Cumulative-strain-damage Model of Ductile Fracture: Simulation and Prediction of Engineering Fracture Tests. Technical Report UCRL-53058. Lawrence Livermore National Laboratory.
- Wu, P.D., Lloyd, D.J., Jian, M., Neale, K.W., Huang, Y., 2007. Effects of spatial grain orientation distribution and initial surface topography on sheet metal necking. *Int. J. Plasticity* 23, 1084–1104.
- Xue, L., 2007. Damage accumulation and fracture initiation in uncracked ductile solids subject to triaxial loading. *Int. J. Solids Struct.* 44, 5163–5181.
- Xue, L., 2009. Stress based fracture envelope for damage plastic solids. *Eng. Fract. Mech.* 76, 419–438.
- Yoon, J.W., Barlat, F., Gracio, J.J., Rauch, E., 2005. Anisotropic strain hardening behavior in simple shear for cube textured aluminum alloy sheets. *Int. J. Plasticity* 21, 2426–2447.
- Yoshida, K., Kuroda, M., 2012. Comparison of bifurcation and imperfection analyses of localized necking in rate-independent polycrystalline sheets. *Int. J. Solids Struct.* 49, 2073–2084.
- Zairi, F., Nait-Abdelaziz, M., Gloaguen, J.M., Lefebvre, J.M., 2011. A physically-based constitutive model for anisotropic damage in rubber-toughened glassy polymers during finite deformation. *Int. J. Plasticity* 27, 25–51.
- Zamiri, A., Pourboghra, F., Barlat, F., 2007. An effective computational algorithm for rate-independent crystal plasticity based on a single crystal yield surface with an application to tube hydroforming. *Int. J. Plasticity* 23, 1126–1147.
- Zhang, F., Bower, A.F., Mishra, R.K., Boyle, K.P., 2009. Numerical simulations of necking during tensile deformation of aluminum single crystals. *Int. J. Plasticity* 25, 49–69. <http://dx.doi.org/10.1016/j.ijplas.2007.12.006>.
- Zhang, M., Zhang, J., McDowell, D.L., 2007. Microstructure-based crystal plasticity modeling of cyclic deformation of Ti–6Al–4V. *Int. J. Plasticity* 23, 1328–1348.
- Zhang, Z.L., Thaulow, C., Odegard, J., 2000. A complete Gurson model approach for ductile fracture. *Eng. Fract. Mech.* 67, 155–168.